Research Square

Preprints are preliminary reports that have not undergone peer review.
They should not be considered conclusive, used to inform clinical practice,
or referenced by the media as validated information.

Wake Dynamics and VIV Suppression Mechanisms of Wavy Cylinders at Subcritical Reynolds Numbers

Malakonda Reddy Lekkala
Universiti Teknologi PETRONAS
Mohamed Latheef
Universiti Teknologi PETRONAS
Do Kyun Kim
do.kim@snu.ac.kr
Seoul National University
Ameen Topa
Universiti Malaysia Terengganu

Research Article

Keywords: Large eddy simulations, hydrodynamic coefficients, wavy cylinders, wavelength ratios, flow characteristics, vibration control

Posted Date: April 16th, 2026

DOI: https://doi.org/10.21203/rs.3.rs-9118810/v1

License: This work is licensed under a Creative Commons Attribution 4.0 International License. Read Full License

Additional Declarations: No competing interests reported.

Wake Dynamics and VIV Suppression Mechanisms of Wavy Cylinders at Subcritical Reynolds Numbers

Malakonda Reddy Lekkala [a, b], Mohamed Latheef [a], and Do Kyun Kim [c d], Ameen Topa [e]

[a] Department of Civil and Environmental Engineering, Universiti Teknologi PETRONAS, Seri Iskandar, Perak, Malaysia

[b] Department of Mechanical and Industrial Engineering, University of Massachusetts Amherst, Amherst, MA, 01003, USA

[c] Department of Naval Architecture and Ocean Engineering, Seoul National University, Seoul, South Korea

[d] Research Institute of Marine Systems Engineering & Institute of Engineering Research, Seoul National University, Seoul, South Korea

[e] Faculty of Ocean Engineering Technology, Universiti Malaysia Terengganu, Kuala Terengganu, Malaysia

Abstract

The wake formations behind wavy cylinders are numerically investigated in this study using large-eddy simulations. The drag force, lift fluctuations, velocity profiles, vortex formation length, and wake pressure coefficient are examined at a Reynolds number ($Re = 3.9 \times 10^3$) based on the mean diameter of the cylinder. Five wavy cylinder models, including single and double wavy configurations, are investigated with wavelength-to-diameter ratios (λ/D_m) ranging from 3.79 to 6.82. The numerical results of the wavy cylinders are compared with those of a smooth circular cylinder having an equivalent diameter. Significant differences in vortical structure patterns are observed between the wavy cylinders and the smooth circular cylinder. Owing to its wavy configuration, the double wavy cylinder achieves maximum reductions in drag and lift coefficients of 14.13% and 89.12%, respectively, compared with the smooth circular cylinder at $\lambda/D_m = 6.06$. This indicates that vortex-induced vibrations can be significantly suppressed at specific combinations of λ/D_m and a/D_m. The wake width of the double wavy (DW) cylinder expands in the downstream region compared with that of the single wavy (SW) cylinder, which in turn is larger than that of the smooth circular (SC) cylinder. The flow separation line along the wavy cylinders varies in the spanwise direction. The free shear layers of the wavy cylinders are more stable and extend further downstream than those of the SC cylinder, rolling up into vortices at a greater downstream distance as λ/D_m increases to 6.06. As a result, the vortex formation length is increased, and lift fluctuations are significantly suppressed through drag reduction. The

fundamental mechanisms of force reduction, including the associated flow features, are discussed for different λ/D_m values.

Keywords: Large eddy simulations, hydrodynamic coefficients, wavy cylinders, wavelength ratios, flow characteristics, vibration control.

1. Introduction

The flow around bluff bodies has been an important problem that has been investigated by many researchers. In fluid mechanics, the flow over bluff bodies is characterized by the formation of vortex shedding in the wake of the body. Various methods were developed to control this vortex shedding, which is mainly responsible for increased drag, noise generation, and vibration of the structure that leads to structural failure. One such flow control method is passive flow control, which is achieved by modifying the cylinder's geometric shape (Choi et al., 2008). In this study, the surface of the slender cylinder is modified to a wavy form along the spanwise direction of the cylinder called a symmetric wavy (SW) cylinder. Many researchers have investigated the effect of geometric modifications on the cylinder flow properties behind the cylinder Assi et al. (2009); Jung and Yoon (2014); Zhuang et al. (2018); Yoon et al. (2020); Lekkala et al. (2022); Lekkala et al. (2023); Deng et al. (2026).

Previous studies have confirmed that the wake formation behind the cylinder can be efficiently modified by altering the cylinders cross-section along the spanwise direction. Choi et al. (2008) have summarized flow control techniques for various cylinder shapes. Ahmed and Bays-Muchmore (1992) carried out investigations to measure the surface pressure distributions and to visualize the flow behind the wavy cylinders at Reynolds number (Re) of $5\times10^3 - 2\times10^4$ with wavelength ratio (λ/D_m) = 1.2, 1.6, 2.0, and 2.4 and fixed wave amplitude ratio (a/D_m) = 0.1. The authors have observed three-dimensional (3D) flow separation lines and trailing of formation of vortices in the streamwise direction. They have also noted that sectional drag coefficient (C_D) is more prominent at the nodes compared to saddle points of the wavy cylinder. Bearman and Owen (1998) changed the leading face of the square cylinder into a wavy form and achieved a maximum C_D reduction of 30% at $Re = 4\times10^4$. Experiments in a wind tunnel at $Re = 2\times10^4 - 5\times10^4$ were carried out by Lam et al. (2004a) to investigate the effects of the waviness of the geometric surface on mean drag coefficient ($\bar{C}_D$), and root mean squared (RMS) lift coefficient ($C_{L,RMS}$) with $\lambda/D_m = 1.45,\ 2.27$ and 2.08 and $a/D_m = 0.09$ and 0.068. The authors have found that the base pressure at any point along the spanwise direction of the SW cylinder is greater than the smooth

circular cylinder at the given Re. The maximum reduction of $\bar{C}_D$ was up to 20% at $\lambda/D_m = 2.27$ and $C_{L,RMS}$ was almost suppressed.

Lam et al. (2004b) extended the study of Lam et al. (2004a) to investigate the near-wake flow of the wavy cylinder using Laser Doppler Velocimetry (LDP). The authors have observed that the length of the vortex formation of the SW cylinder is longer than the SC cylinder, which leads to minimizing $\bar{C}_D$ and suppressing the vortices. The authors have concluded that as the Re increases, the vortex formation length (L_{FC}) of the SC cylinder decreases, whereas the L_{FC} of SW cylinder increases. Zhang et al. (2005) used Particle Image Velocimetry (PIV) to study the 3D wake structures behind the symmetric wavy (SW) cylinder at $Re = 3\times10^3$. The authors have observed alternative vortices along the spanwise direction of the cylinder. This resulted in the suppression of long vortices and minimized the turbulent kinetic energy behind the cylinder. They have also concluded that geometric surface modification to wavy form greatly influences the near-wake vortex formation and governs 3D vortices. At the same time, Lee and Nguyen (2007) investigated the flow behind wavy cylinders for different wavelengths for Re in the range of $5\times10^3 - 2\times10^4$. The authors observed that the wake width decreased downstream of nodal planes and increased downstream of saddle planes. They have also found that the vortex formation lengths are elongated for wavy cylinders, reducing the drag by 22% and suppressing the lift fluctuations.

A range of SW cylinders with combinations of λ/D_m and a/D_m was investigated by Lam and Lin (2007) at the laminar flow regime ($Re = 100$). The authors have observed that free shear layers behind the SW cylinders are more resistant to roll to form vortices, enabling them to develop longer L_{FC} compared to SC cylinders. They have concluded that as a/D_m increases, a larger reduction in force coefficients is observed. In contrast, Lam and Lin (2008) investigated the flow around SW cylinder at $Re = 3\times10^3$ with $\lambda/D_m = 1.136 - 3.333$ and a fixed $a/D_m = 0.152$ using large-eddy simulations (LES). An optimal $\lambda/D_m = 1.90$ was provided at which the maximum reduction in $\bar{C}_D$ was achieved. Lin et al. (2016) extended the work of Lam and Lin (2008) to examine flow properties behind the wavy cylinder for higher $\lambda/D_m = 3.79 - 7.57$ at $Re = 3\times10^3$ using LES. Based on this λ/D_m, the authors have categorized the flow into three regimes, namely: (i) regime I ($\lambda/D_m < 6.0$), (ii) regime II ($\lambda/D_m \approx 6.0$), and (iii) regime III ($\lambda/D_m > 6.0$). At optimum $\lambda/D_m = 6.06$, the maximum reduction in $\bar{C}_D$ is up to 16% and $C_{L,RMS}$ is around 93%. They have also concluded that the L_{FC} at the node is longer than the saddle at optimum λ/D_m. From Lam

and Lin (2008) and Lin et al. (2016) studies, it can be observed that two distinct optimal λ/D_m exist, one each for $\lambda/D_m < 3.57$ and $\lambda/D_m > 3.57$. Deng et al. (2026) performed water tunnel experiments and LES simulations to investigate the performance of hydrodynamic coefficients of seal whiskers at $Re = 3\times10^3$ and found that wavy elliptic cylinders with $\lambda/D_m = 3$ and 4 reduced the mean drag and lift y 12.5: and 86.6% respectively when compared with straight elliptic cylinders. Whereas for the same Re number, Lekkala et al. (2023) concluded that DW cylinder reduced the drag and lift coefficients by 16.63% and 94.99% for $\lambda/D_m = 6.06$ compared to SC cylinder.

Using LES, Lin and Lin (2009) conducted a numerical investigation of flow around the SW cylinder and validated the results with load cell measurements at $Re = 3\times10^3$. The authors have found that 3D free shear layers behind the SW cylinder are more stable than 2D shear layers. These 3D shear layers matured into vortices downstream of the cylinder, modifying the pressure distributions and wake structures, in agreement with Zhang et al. (2005). At $Re = 100$, Zou et al. (2013) investigated the spacing between two SW cylinders in a tandem arrangement with a spacing ratio (L/D_m) ranging from 1.5 to 5.5 considering the 3D laminar flow regime. A significant reduction in $\bar{C}_D$ and suppression of $C_{L,RMS}$ for both cylinders was effectively observed for $L/D_m > 4.0$. Zhao et al. (2011) adopted a scale-adaptive simulation model (SAS) to investigate the flow around the SW cylinder $Re = 8\times10^3$ for $\lambda/D_m = 3.0-7.0$ and $a/D_m = 0.091-0.25$. The SW cylinder reduced the $\bar{C}_D$, Strouhal number (St) and $C_{L,RMS}$ by 30%, 50%, and 92%, respectively, compared to the SC cylinder at optimal $\lambda/D_m = 5.0$ and $a/D_m = 0.25$. When the λ/D_m ranges between 5.0 and 7.0, the free shear layers become steadier and roll into mature vortices further downstream of the cylinder. For λ/D_m ranges between 5.0 and 7.0, the free shear layers become steadier and roll into developed vortices further downstream of the cylinder.

A series of cylinders with different geometric modifications were investigated by Zhang et al. (2016) using LES at $Re = 5.0\times10^3$. This study includes five cases: two 2D cross-sectional changes (polygonal and ridged) and three 3D dimensional spanwise modifications (linear wavy, sinusoidal wavy, and O-ringed). The authors have found that polygonal and ridged cylinders have a negligible effect on the flow characteristics when compared with linear wavy and sinusoidal wavy cylinders. Karthik et al. (2020) investigated the impact of geometric waviness on the drag and sound of the bluff bodies at $Re = 9.73\times10^4$ using LES. The authors found that at optimum $\lambda/D_m = 1.892$ and $a/D_m = 0.134$, $\bar{C}_D$ and sound by a wavy cylinder was reduced by 33.21% and 6.331 dB, respectively, compared to a smooth circular cylinder. A recent study by Zhang et al.

(2021) investigated the flow behind the double wavy (DW) cylinder using LES with $\lambda/D_m = 1.80-5.0$ and $a/D_m = 0.05-0.2$ at $Re = 3.9\times10^3$. The authors have observed that as a/D_m increases, the amount of reduction in $\bar{C}_D$ increases gradually compared to the SC cylinder, and the maximum reduction of 13% occurred at $a/D_m = 0.2$. A similar trend was observed for $C_{L,RMS}$ with a maximum decrease of 94% compared to the SC cylinder at $\lambda/D_m = 2.0$ and $a/D_m = 0.2$. The authors have noticed that the mean velocity distribution changes from a symmetric U-shaped profile to a V-shaped profile further downstream of the cylinder. Chen et al. (2022) studied the noise and flow control mechanisms of wavy cylinders for different Re. The authors found that noise radiation was reduced and that tones were suppressed by the wavy cylinder compared to the circular cylinder.

From the above research, the experimental and numerical simulations were mainly concentrated at $Re = 3.9\times10^3$ or lower with low λ/D_m by most of the researchers, because it could better capture the flow properties behind the cylinders at sub-critical Re number. However, the previous work has been limited to λ/D_m between 1.80 to 5.0. The current study aims to capture the effect of higher $\lambda/D_m = 3.79-6.82$ at $Re = 3.9\times10^3$ and estimate the optimum λ/D_m of DW and SW cylinders. In addition, the flow properties of the DW cylinder are compared with SW and SC cylinders. The flow-induced force coefficients such as mean drag and RMS lift coefficients, Strouhal number (St), and 3D vortex structures are discussed in this study. This paper is organized as follows: Section 2 presents the computational, numerical details, and validation studies of flow around SC, SW, and DW cylinders. The grid dependence study is also offered in Section 2. The mechanism of flow characteristics, with results and discussions, is shown in Section 3. Finally, in Section 4, the conclusions and further recommendations are summarized.

2. Numerical methodology details

2.1 Numerical aspects of governing equations

The present study adopts the incompressible Navier-Stokes equations with LES turbulence model to solve the flow behind the cylinder, and the governing equations are described below:

$$\frac{\partial \bar{u}_i}{\partial t} + \frac{\partial \overline{u_i u_j}}{\partial x_j} = -\frac{\partial \bar{p}}{\partial x_i} + \frac{1}{Re}\frac{\partial^2 \bar{u}_i}{\partial x_j \partial x_j} - \frac{\partial \tau_{ij}}{\partial x_j}, \qquad (i = 1, 2, 3) \tag{1}$$

$$\frac{\partial \overline{u_i}}{\partial x_i} = 0 \tag{2}$$

Where $\bar{u}_i$ or $\bar{u}_j$ (i=1, 2, 3) represent the filtered velocity components in the Cartesian coordinates in x_i (or x_j) direction. $\bar{p}$ is the pressure and τ_{ij} is the subgrid-scale stress component defined as $\tau_{ij} = \overline{u_i u_j} - \overline{u_i u_i}$.

The eddy-viscosity model is used in the sub-grid scale (SGS) model, and the anisotropic portion of the SGS model stress tensor has the following form:

$$\tau_{ij}^a = \tau_{ij} - \frac{1}{3}\tau_{kk}\delta_{ij} = -2\nu_T \overline{S_{ij}} \tag{3}$$

Smagorinsky (1993) proposed the most extensively used eddy-viscosity model, which is employed in this study and defined as follows:

$$\nu_T = (C_S \Delta)^2 \left|\bar{S}\right| \tag{4}$$

Where Δ is the filter width and defined as $\Delta = (\Delta_1, \Delta_2, \Delta_3)^{1/3}$ (Deadroff, 1970), and Δ_1, Δ_2, and Δ_3 presents the sizes of the computational cells. $\left|\bar{S}\right| = (2\overline{S_{ij}}\,\overline{S_{ij}})^{1/2}$ featuring as $\overline{S_{ij}} = ((\partial \overline{u_i}/\partial x_j) + (\partial \overline{u_j}/\partial x_i))/2$ and C_S is the Smagorinsky constant.

This study adopts a dynamic Smagorinsky (SGS) model proposed by Germano et al. (1991) to represent an unresolved sub-grid scale fluid motion. The second filter is set and applied to large-eddy as specified in Eq. (1):

$$T_{ij} = \overline{u_i u_j} - \bar{\bar{u}}_i \bar{\bar{u}}_j \tag{5}$$

$$L_{ij} = \overline{u_i}\,\overline{u_j} - \bar{\bar{u}}_{ij} \bar{\bar{u}}_j \tag{6}$$

The stresses are represented using the Germano identity as follows:

$$L_{ij}^a = T_{ij}^a - \hat{\tau}_{ij}^a \tag{7}$$

where

$$T_{ij}^a = -2(C_S \hat{\Delta})^2 |\bar{\bar{S}}| \bar{\bar{S}}_{ij} \tag{8}$$

Here $\hat{\Delta}$ is defined as the characteristic filter width associated with the test filter. Finally, the following equation may be used to obtain a space- and time-dependent Smagorinsky coefficient. :

$$(C_s\Delta)^2 M_{ij} = L_{ij}^a \tag{9}$$

$$\text{where } M_{ij} = -2\left(\frac{\bar{\Delta}}{\Delta}\right)^2 |\bar{S}|\bar{S}_{ij} + 2|\bar{S}|\bar{S}_{ij} \tag{10}$$

More information on the present SGS model may be found in Yoon et al. (2009) and Jung and Yoon (2014). Jung and Yoon (2014) have already successfully used the Smagorinsky SGS model to investigate the flow over a helically twisted cylinder at the same Re used in this research.

2.1 Numerical schemes

The above equations are solved using OpenFOAM, which employs a finite-volume scheme. The coupling between pressure and velocity is resolved by using the Pressure-Implicit with Splitting of Operators (PISO) algorithm. A second-order Adams-Bashforth scheme is used for the discretization of convective terms, and the Crank-Nicolson scheme is used for the diffusive term. For momentum discretization, a second-order central differencing scheme is used while the two-step time split scheme is adopted for temporal discretization, and Poisson's equation solution satisfy the continuity equation. The convergence criteria for the residuals and other equations are set to 10^{-4} and 10^{-5}, respectively. The aforementioned numerical methodology was successfully used by Jung and Yoon (2014).

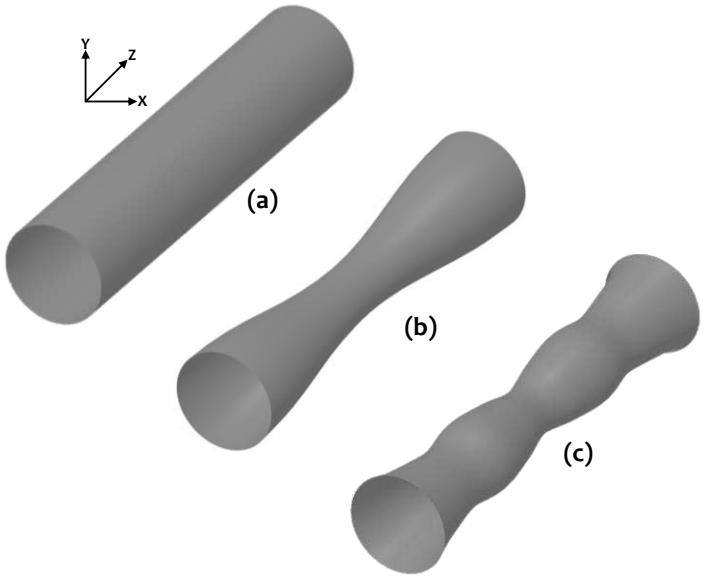


Fig. 1. The geometry of the cylinders (a) smooth circular (SC), (b) symmetric wavy (SW), and (c) double wavy (DW) cylinders.

2.2Geometric definition of the cylinders

The geometric shapes of the smooth circular (SC), symmetric wavy (SW), and double wavy (DW) cylinders investigated in this study are shown in Fig. 1. The local diameter of the SW cylinder is based on the following equation:

$$D_Z = D_m + 2a\cos\left(\frac{2\pi z}{\lambda_1}\right) \tag{11}$$

where D_m represents the average of the maximum (D_{max}) and minimum diameters (D_{min}) of the SW cylinder. The diameter of the SC cylinder and the mean diameter of the SW cylinder is the same in this study. The notations presented in Fig. 2 as N(node), M(middle), S(saddle) are equivalent to local D_{max}, D_m and D_{min} respectively. The wavelength and amplitude of the cylinders are represented by λ_1 and 'a' respectively. In this study, the flow behind the SC cylinder is considered as a base case for comparison with the flow behind SW and DW cylinders.

The DW cylinder is defined with two wavelengths, as stated in Eq. (12), and the geometry is shown in Fig. 2.

$$D_Z = D_m + a\left[\cos\left(\frac{2\pi z}{\lambda_1}\right) + \cos\left(\frac{2\pi z}{\lambda_2}\right)\right] \tag{12}$$

The wavelength λ_2 is perceived as an $\lambda_1/3$ of the SW cylinder. The DW cylinder has a total of four saddles and four-node points along its length.

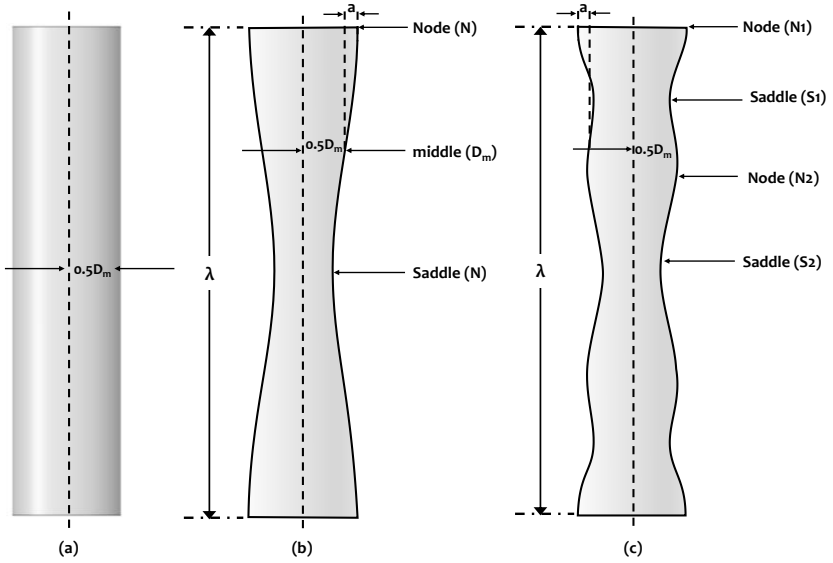


Fig. 2. Schematic of the simulated (a) SC (b) SW (c) DW cylinders.

2.3 Computational boundary conditions, grid size, and validation studies

The detail of the computational grid is presented in Fig. 3. O-grid is adopted in this study with a far-field at a distance of $20D_m$ from the center of the cylinder, as shown in Fig. 3. The uniform flow speed and a convective boundary condition ($(\partial u_i/\partial t)+(c\partial u_i/\partial x)=0$) are defined at inlet and outlet boundaries, respectively. A Neuman boundary condition is applied at the outlet boundary for the pressure outlet region. At the cylinder surface, no-slip and no-penetration boundary conditions are applied. The details of the various combinations of λ/D_m and a/D_m cylindrical models and the gird sizes used in this study are presented in Table 1.

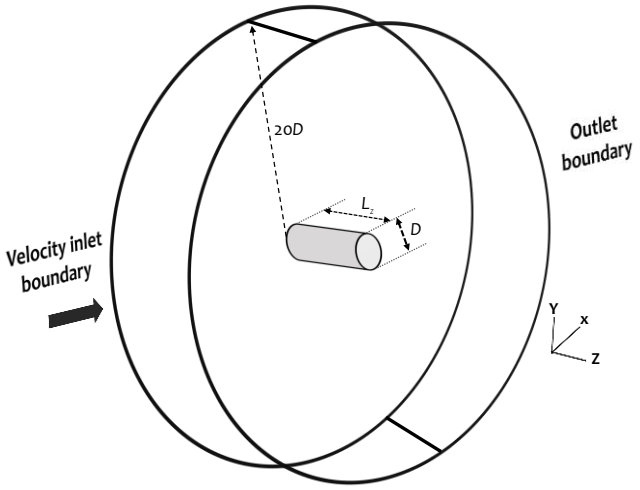


Fig. 3. Representation of the Flow domain and boundary conditions.

Table 1. Particulars of the cylinder models.

Model	λ/D_m	a/D_m	$N_r \times N_\theta \times N_z$	Domain size ($L_x \times L_y \times L_z$)
1	3.79	0.152	268x222x70	20x20x3.79
2	4.55	0.152	268x222x82	20x20x4.55
3	5.30	0.152	268x222x94	20x20x5.30
4	6.06	0.152	268x222x106	20x20x6.06
5	6.82	0.152	268x222x118	20x20x6.82

To validate the current numerical methodology adopted in the current study, the mean drag coefficient ($\bar{C}_D$), fluctuating lift coefficient ($C_{L,RMS}$), and Strouhal number (St) are compared with the published experimental and numerical simulation results. The grid-dependence test has been carried out to assess the effect of grid size on the results.

The drag (C_D) and lift coefficients (C_L) measured in this study are defined as:

$$C_D = \frac{2F_D}{\rho U_\infty^2 D_m L} \tag{13}$$

$$C_L = \frac{2F_L}{\rho U_\infty^2 D_m L} \tag{14}$$

where F_D is the total drag force, and F_L is the lift force acting on the cylinder. ρ and U_∞ are density and free stream velocity of the fluid flow, respectively. L is the spanwise length of the cylinder.

The Strouhal number that defines the frequency of the vortex shedding (F_s) and is specified as:

$$St = \frac{F_s D_m}{U_\infty} \tag{15}$$

Before performing detailed numerical simulations, it is critical to validate the numerical model. At first, three different grid sizes, as presented in Table 2, are used to carry out the grid dependency test by considering the precision of the computational results using LES with regards to gird resolution requirements near the wall of the cylinder, the grid is clustered to solve the viscous sub-layer of the region in the near-wall of the cylinder equivalent to the distance to the closest mesh points fixed at $y^+ \leq 1.0$, and the spacing is augmented at a ratio of 1.10 farther from cylinder surface walls. The non-dimensional time step is set to 0.001 to ensure the Courant-Friedrichs-Lewy (CFL) condition is less than 1.0 throughout the simulations. In the current simulations, three unique cylinder models with varying grid cells are used for SC and DW cylinders, as presented in Table 2. These three grid systems are composed of 4.40, 5.60, and 7.08 million grids, respectively. The flow around SC and DW cylinders at $Re = 3.9 \times 10^3$ is compared with the experimental and numerically simulated results from the literature. The three grids have almost the same outcome. As presented in Table 2, for the SC cylinder, the mean drag coefficient ($\bar{C}_D$) from the present LES agrees well with numerical simulations using LES by Lam et al. (2010) and Zhang et al. (2021) and is close to the experimental work by Lubcke et al. (2001) and numerical studies by Franke and Farnk (2002). The root mean square (RMS) lift coefficient ($C_{L,RMS}$) is well in range with summarized studies in Table 2. The Strouhal numbers (St) calculated in this study agree well with results from both numerical (LES) and experimental studies carried out by different researchers. The exact gird sizes are used to investigate the flow behind the DW cylinder at 3.9×10^3 with $\lambda / D_m = 5.30$ and $a / D_m = 0.152$. The $\bar{C}_D$, $C_{L,RMS}$, and St of DW cylinder for medium and fine grids converged and are consistent with the numerical results by different

investigators from the literature as presented in Table 2. Consequently, in the present LES calculations, a fine grid is used for the SW and DW cylinder cases.

Table 2. Grid dependency analysis and force coefficients comparison with experimental and numerical simulation results for SC and DW cylinders.

Geometry	Case	Re	$N_r \times N_\theta \times N_z$	$\bar{C}_D$	$C_{L,RMS}$	St
SC	Lubcke et al. (2001)	3.9×10^3	Experimental	0.990	----	0.215
	Lam et al. (2010)	3.9×10^3	Numerical	1.073	0.1640	0.207
	Franke and Frank (2002)	3.9×10^3	Numerical	0.994	----	0.209
	Zhang et al. (2021)	3.9×10^3	Numerical	1.085	0.2663	0.209
	Coarse	3.9×10^3	240 x 198 x 72	1.182	0.1962	0.207
	Medium	3.9×10^3	252 x 210 x 84	1.126	0.1882	0.211
	Fine	3.9×10^3	268 x 224 x 94	1.093	0.1865	0.212
DW	Zhao et al. (2011)	8.0×10^3	Numerical	0.869	0.0303	0.1474
	Lam et al. (2010)	3.9×10^3	Numerical	0.922	0.0210	0.179
	Zhang et al. (2021)	3.9×10^3	Numerical	0.929	0.0136	----
	Coarse	3.9×10^3	240 x 198 x 72	0.968	0.0227	0.188
	Medium	3.9×10^3	252 x 210 x 84	0.945	0.0211	0.189
	Fine	3.9×10^3	268 x 224 x 94	0.936	0.0203	0.191

Likewise, by using the grid from Table 1, the flow behind SW and DW cylinders at $Re = 3.9\times10^3$ with $\lambda/D_m = 3.79 - 6.82$ and $a/D_m = 0.152$ is investigated in the following sections. The flow features around SW and DW cylinders are compared with SC cylinders, and an attempt is made to present the optimal λ/D_m at $Re = 3.9\times10^3$.

3 Results and Discussion

3.1 Force coefficients and Strouhal number

The primary objective of this study is to investigate the effect of λ/D_m on hydrodynamic coefficients and flow features of the SW and DW cylinders. Also, to find the optimal λ/D_m, that can lower the drag and lift fluctuations and suppress the vortex shedding simultaneously. The predicted force coefficients of flow behind the SC, SW, and DW cylinders are presented in Figs. 4 and 5. To validate the present methodology, the force coefficients $\bar{C}_D$ and $C_{L,RMS}$ of SC and DW are compared with results from Zhang et al. (2021) for $\lambda/D_m = 5.30$, as presented in Table 2. These force coefficients of the SC and DW cylinders are consistent with Zhang et al. (2021). At $Re = 3.9\times10^3$, for $\lambda/D_m = 5.30$, the SW cylinder reduced the $\bar{C}_D$ and $C_{L,RMS}$ by 10.61% and 84.49% respectively compared to SC cylinder as presented in Table 3.

In comparison, for the DW cylinder, the $\bar{C}_D$ was reduced by 3.94% and 14.13% compared to SW and SC cylinders, respectively. Additionally, the DW cylinder almost suppressed lift fluctuations by 29.86% and 89.12% compared to SW and SC cylinders, respectively, a result not previously reported in the literature. It can be inferred that the DW cylinder effectively reduces the fluid forces compared to SW and SC cylinders.

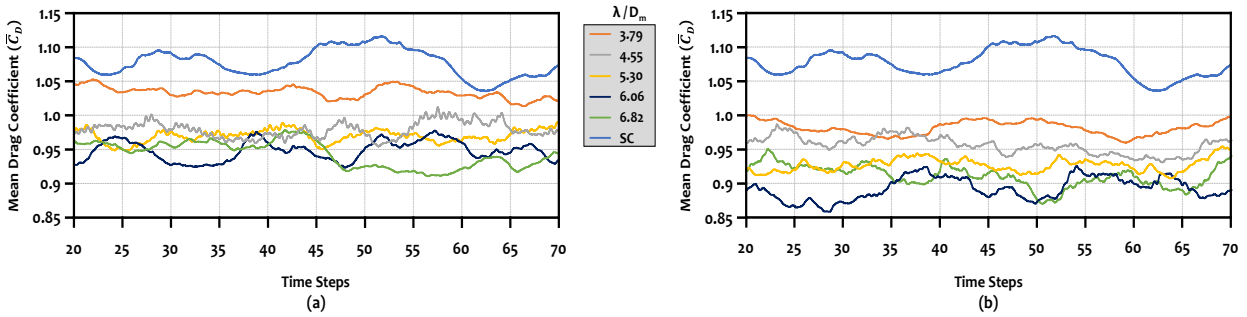


Fig. 4. Comparison of drag coefficients (a) SW cylinders, and (b) DW cylinders at $Re = 3.9 \times 10^3$.

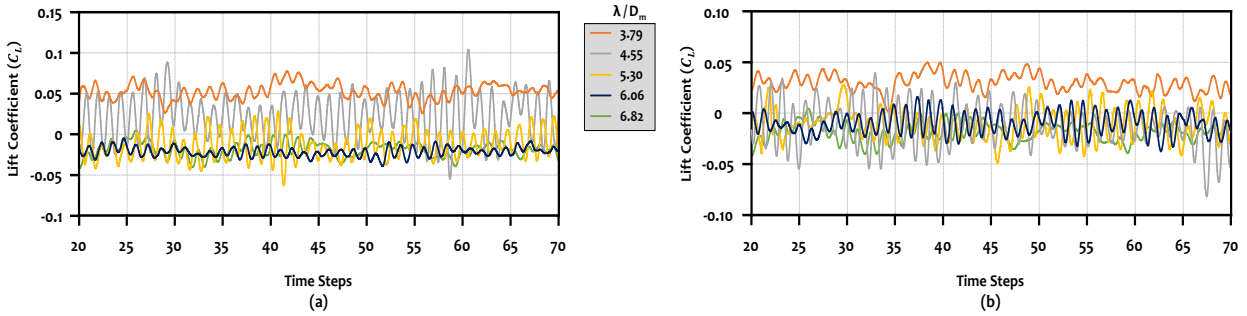


Fig. 5. Comparison of lift coefficient (a) SW cylinders, and (b) DW cylinders at $Re = 3.9 \times 10^3$.

Table 3. Comparison of $\bar{C}_D$ and $C_{L,RMS}$ at $Re = 3.9 \times 10^3$ and $\lambda / D_m = 5.30$.

Cylinder	$\bar{C}_D$	% of diff.	$C_{L,RMS}$	% of diff.
SC	1.109	---	0.1865	---
SW	0.974	-10.61	0.0289	-84.49
DW	0.936	-14.13	0.0203	-89.12

To estimate the Strouhal number, Fourier transforms are applied to the time history of C_L. The St of SC, SW, and DW cylinders are shown in Fig 6. The St of DW cylinder is more petite when compared to SW and SC cylinders, as shown in Fig. 6. The variation of the St with λ / D_m follows a similar trend as the $\bar{C}_D$ and $C_{L,RMS}$. As λ / D_m increases, the St significantly reduces. This kind of behavior was observed by Zhao et al. (2011) at $Re = 8.0 \times 10^3$ with $a / D_m = 0.25$. This

confirms that the vortex-induced vibrations (VIV) can be effectively alleviated by using wavy configurations. These observations agree well with Lam et al. (2010) and Zhao et al. (2011).

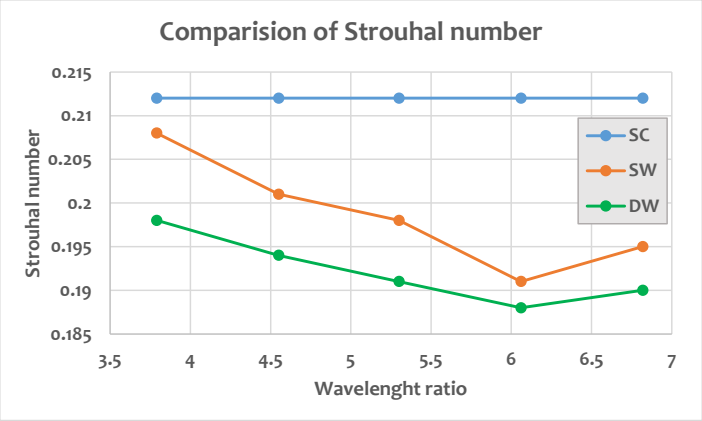


Fig. 6. Variation of Strouhal number for different wavelength ratios for SC, SW, and DW cylinders with $a/D_m = 0.152$ at $Re = 3.9\times10^3$.

Figs. 7 and 8 present the variation of $\bar{C}_D$ and $C_{L,RMS}$ for SW and DW cylinders for different λ/D_m, respectively. For comparison purposes, the $\bar{C}_D$ and $C_{L,RMS}$ of SC is also presented in Figs. 7 and 8, respectively. From Fig. 7, it can be noted that as λ/D_m increases, the $\bar{C}_D$ of SW and DW gradually decrease up to $\lambda/D_m = 6.06$ and then increases to $\lambda/D_m = 6.82$. The maximum and minimum values of $\bar{C}_D$ occurred at $\lambda/D_m = 3.79$ and $\lambda/D_m = 6.06$ respectively for both SW and DW cylinders. At $\lambda/D_m = 3.79$, $\bar{C}_D$ was reduced by 4.03% and 9.55% by SW and DW cylinder respectively when compared to SC. Whereas at $\lambda/D_m = 6.82$, when compared to SC, the $\bar{C}_D$ was reduced by 11.36% and 15.84% by SW and DW cylinders, respectively. But the maximum reduction of $\bar{C}_D$ occurred at $\lambda/D_m = 6.06$ by 12.46% and 17.53% by SW and DW cylinders, respectively.

A similar trend can be observed for $C_{L,RMS}$, as demonstrated in Fig. 8. The minimum and maximum reductions took place at $\lambda/D_m = 3.79$ and $\lambda/D_m = 6.06$ respectively for both SW and DW cylinders. The lift fluctuations were almost suppressed by the DW cylinder at $\lambda/D_m = 6.06$ than the SW cylinder when compared to SC. The percentage of the difference between SC, SW, and DW cylinders force characteristics for each λ/D_m is presented in Fig. 9. It is possible to conclude that for each λ/D_m, DW cylinders provided more reduction in $\bar{C}_D$ and $C_{L,RMS}$ than SW

cylinders; both being lower when compared to SC. Among DW cylinders with different wavelength ratios, $\lambda/D_m = 6.06$ provided more reduction compared to other wavelength ratios.

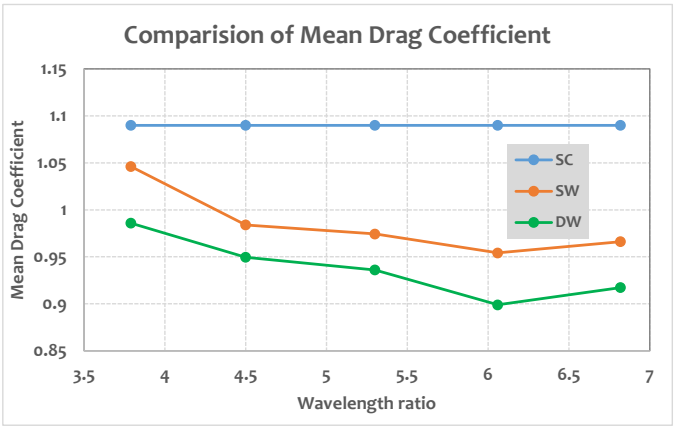


Fig. 7. Variation of mean drag coefficient for different wavelength ratios for SC, SW, and DW cylinders with $a/D_m = 0.152$ at $Re = 3.9\times10^3$.

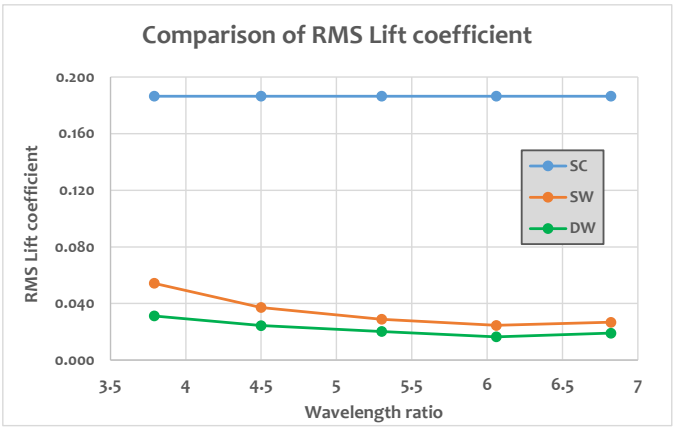


Fig. 8. Variation of RMS lift coefficient for different wavelength ratios for SC, SW, and DW cylinders with $a/D_m = 0.152$ at $Re = 3.9\times10^3$.

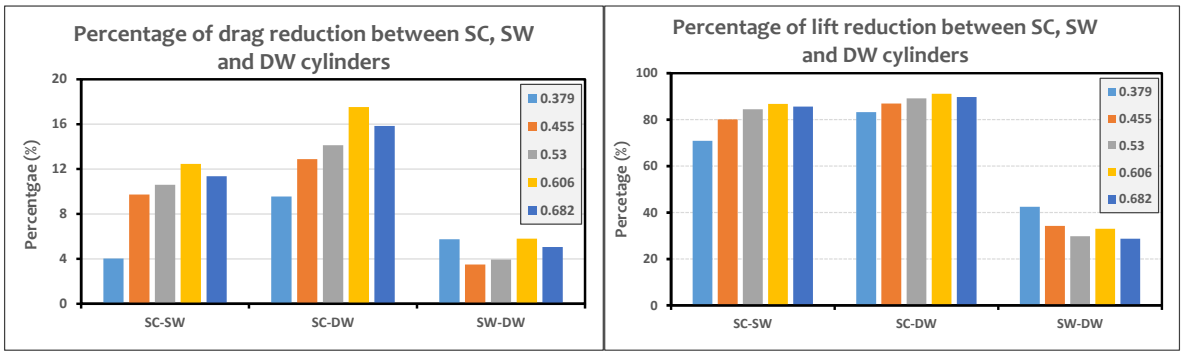


Fig.9. Comparison of percentage of the difference between $\bar{C}_D$ and $C_{L,RMS}$ for SC and SW cylinders at $Re = 3.9 \times 10^3$ for different wavelength ratios.

3.2 Flow structure patterns

The instantaneous iso-surface of the flow fields for different configurations of SC, SW, and DW cylinders are demonstrated in Figs. 10 and 11 respectively for different λ / D_m at $Re = 3.9 \times 10^3$. These iso-surfaces are visualized using the Q criterion where Q=1.0 (Jeong and Hussain 1995). It can be observed that the vortex rolled up immediately in the wake of a smooth circular cylinder, whereas it did not in the SW and DW cylinders. This vanishing of vortex shedding and delay in vortex roll-up in the near wake of SW and DW cylinders can be explained by evaluating the swirl strength of SC cylinders, as shown in Figs. 10 and 11. These findings on the flow control method using the geometric wavy surface of cylinders are consistent with those of Zhang et al. (2005), Xu et al. (2010), Jung and Yoon (2014), Lin et al. (2016), and Yoon et al. (2017).

The SC cylinder evidently showed the presence of shear layers firmly rolling up to form large-scale von Karman vortices in the cylinder's near wake region, as presented in Fig. 10. A wavy fashioned flow was observed along the spanwise direction, which indicates the development of 3D shear layers. A similar development of shear layers in the wake of the cylinder was seen by Yoon et al. (2017) and Lin et al. (2016). The SW and DW cylinders exhibited similar vortical structures downstream of the cylinders. In the wake of cylinders, the vortices formed by SW and DW cylinders are broader in spanwise areas, causing a delay in the vortices roll-up. The vortical structures of the DW cylinder delayed the roll-up of vortices relative to those of the SW and SC cylinders. The delayed rolling up of the vortices elongated the shear layer in the wake of DW cylinders, leading to the vanishing of vortex shedding, as shown in Fig. 11, and resulting in longer vortex formation lengths. These vortices produced by geometric surface modifications of the cylinders demonstrate the presence of periodicity along its spanwise orientations and play a part in altering vortical structures in the closest wake of the cylinders. From Fig. 11, it can be noted that the length of the separated shear layer at saddle planes are longer than the nodal planes for all λ / D_m for DW cylinder, but which is vice versa for SW cylinders. A rib-like structure joining the neighboring vortices in the wake of the cylinders is observed in all cases for SW and DW cylinders, consistent with Gerrard (1978). Based on these interpretations, it can be established that the wavy-shaped cylinders produced flow structures different from those of the SC cylinder. The spanwise formation of vortices and their roll-up strongly depend upon the wavelength of the cylinders. It may be deduced that the transformation and rolling of vortex patterns are sensitive to surface geometry, and that the control mechanism of the vortex structure patterns of the

cylinders is influenced by it. It can be concluded that the strong 3D flow structures behind the cylinders are related to the body's surface geometry, which is also observed by Lee and Nguyen (2007).

As the λ/D_m increased, the length of the separated shear layer attached to the cylinder increased until $\lambda/D_m = 6.06$ and then decreased for $\lambda/D_m = 6.82$ for both SW and DW cylinders, as shown in Fig. 10 and 11. The vortices generated in the streamwise direction in the near wake are more stabilized for $\lambda/D_m = 6.06$ than in other cases for SW and DW cylinders, which delayed the rolling into matured vortices leading to the formation of an elongated separated shear layer and longer vortex formation length. DW cylinder with $\lambda/D_m = 6.06$ showed more stabilized vortices in the wake of the cylinder than the SW cylinder and rolled up into matured vortices further downstream, which resulted in the increase of the base pressure and reduction in fluctuations. This leads to a reduction in $\bar{C}_D$ and $C_{L,RMS}$ for SW and DW cylinders.

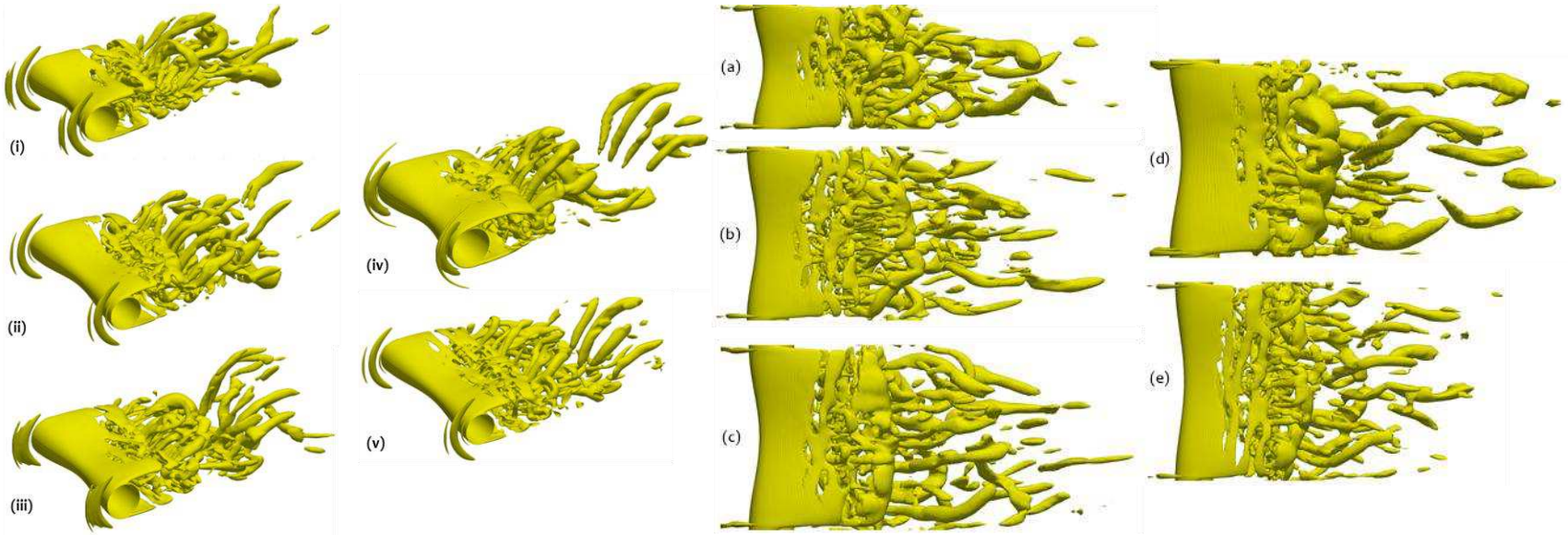


Fig. 10. Instantaneous iso-surfaces of flow around the SW cylinder for (i), (a) - $\lambda/D_m = 3.79$, (ii) , (b) - $\lambda/D_m = 4.05$, (iii), (c) - $\lambda/D_m = 5.30$, (iv), (d) - $\lambda/D_m = 6.06$ and (v), (e) - $\lambda/D_m = 6.82$ at $Re = 3.9 \times 10^3$.

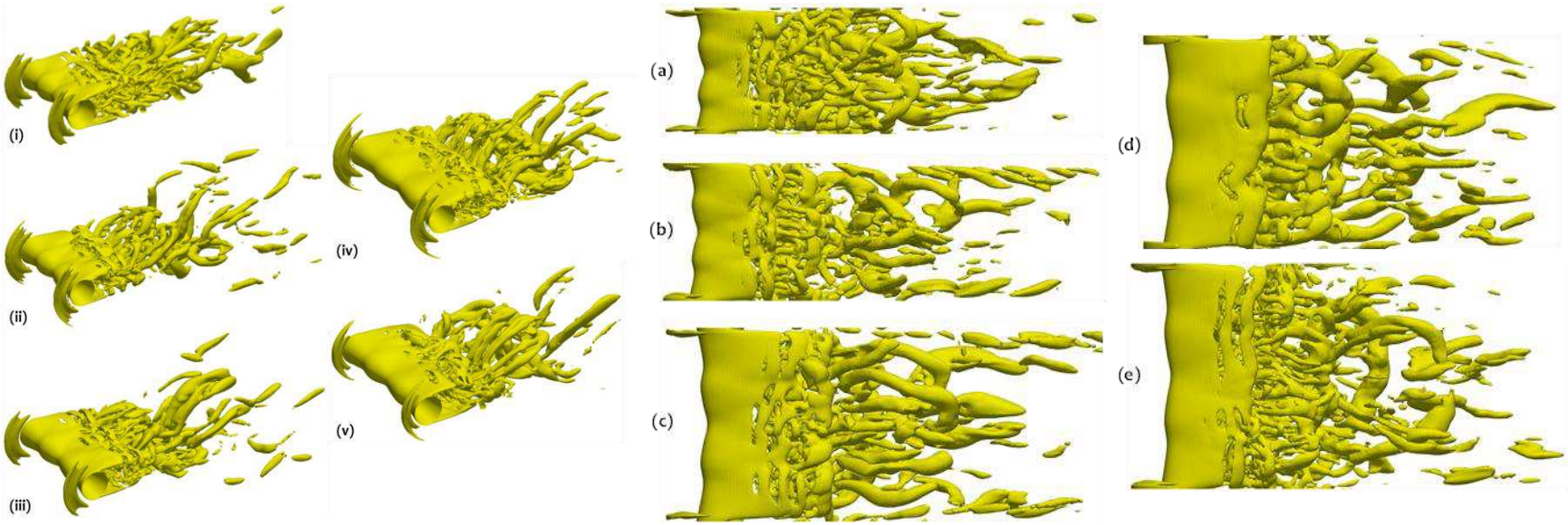


Fig. 11. Instantaneous iso-surfaces of flow around the DW cylinder for (i), (a) - $\lambda/D_m = 3.79$, (ii) , (b) - $\lambda/D_m = 4.05$, (iii), (c) - $\lambda/D_m = 5.30$, (iv), (d) - $\lambda/D_m = 6.06$ and (v), (e) - $\lambda/D_m = 6.82$ at $Re = 3.9 \times 10^3$.

3.3 Velocity distributions

It is essential to analyze the velocity distributions in the cylinders' wake regions to better understand the flow mechanisms. The mean longitudinal velocity distributions ($\bar{u}/U_\infty$) along the centerline of the wake for SW and DW cylinders for different λ/D_m at $Re = 3.9\times10^3$ are presented in Fig. 12 and Fig. 13, respectively. For comparison, a smooth circular cylinder is presented in Fig. 12, and for validation purposes of the present results, the $\bar{u}/U_\infty$ of $\lambda/D_m = 5.30$ were compared with published results by Zhang et al. (2021) at $Re = 3.9\times10^3$ with $\lambda/D_m = 5.0$ and $a/D_m = 0.15$. A small discrepancy can be noticed between the present and other published results, which are assigned to an all-encompassing effect associated with a noticeable difference in amplitude ratio, calculation method, etc.,

It can be observed that the wake flow of the cylinders starts to change from streamwise flow to reverse flow at $x/D_m = 0.5$ and reached a minimum as low as $\bar{u}/U_\infty = -0.5$ and gradually increases to 0.85-0.9 at $x/D_m = 7.0$. For SW cylinders, some interesting characteristics could be observed. Firstly, the negative velocity range (reverse flow region) at nodal planes is longer than the saddle planes and both of these are significantly longer than the smooth circular cylinder, which agrees well with Lam et al. (2010) and Lin et al. (2016). Whereas for DW cylinders, the negative velocity range at nodal planes is smaller than the saddle planes as shown in Fig. 13, which agrees well with Chen et al. (2022). Moreover, it can be observed that for SW and DW cylinders, the $\bar{u}/U_\infty$ for $\lambda/D_m = 6.06$ differ largely from other cylinder configurations and SC cylinders. Meaning that for $\lambda/D_m = 6.06$, SW and DW cylinders demonstrate large reverse flow regions and longer vortex formation lengths than other configurations. At $\lambda/D_m = 6.06$, DW cylinder at saddle plane exhibits longer reverse flow region than nodal planes of DW cylinder and nodal, saddle planes of SW cylinder. This indicates that the flow field at $x/D_m = 3.41$ for the DW cylinder with $\lambda/D_m = 6.06$ exhibits strong 3D flow features due to lengthening and deformations of vortices in the separated shear layers downstream of the cylinder as shown in Fig. 11(a)(iv) and Fig. 11(b)(iv). From Figs. 12 and 13, distributions of $\bar{u}/U_\infty$ for the SW and DW cylinders show the semi-symmetric trend of V- and U-shaped velocity profiles and eventually converge at the same level as smooth circular cylinder at $x/D_m = 7.0$ and $x/D_m = 6.0$ respectively. It can be observed that the variation of $\bar{u}/U_\infty$ strongly depend upon the geometric surface of the cylinders. Based on the point

where the $\bar{u}/U_\infty$ reverses and reaches zero, the vortex formation lengths are measured which are explained briefly in Section 3.4.

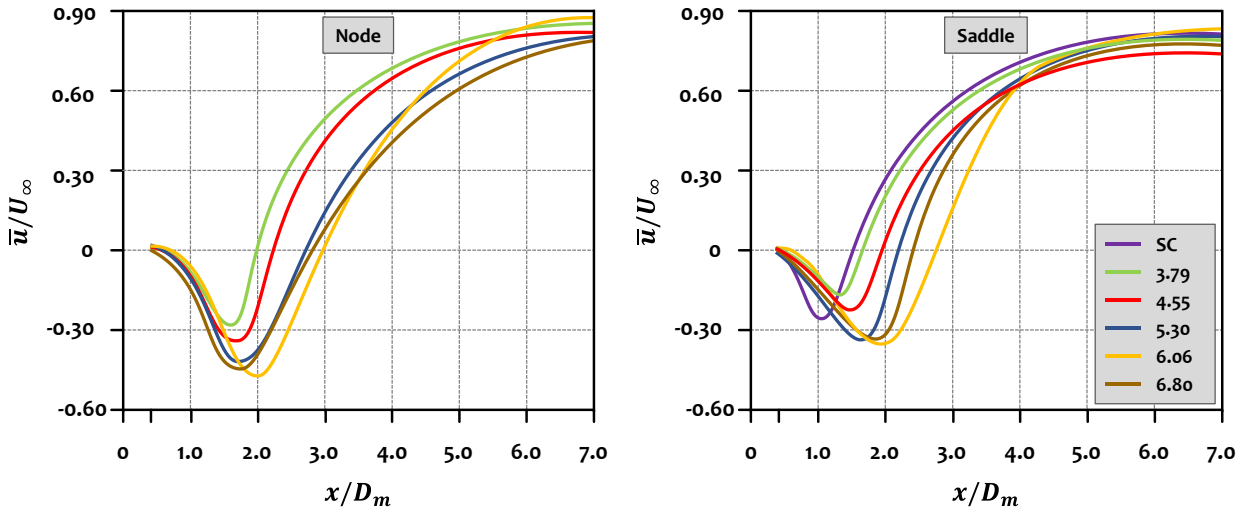


Fig. 12. Mean streamwise velocity distributions along the centerline of the SW cylinder for $\lambda/D_m = 3.79-6.82$ at $Re = 3.9\times10^3$.

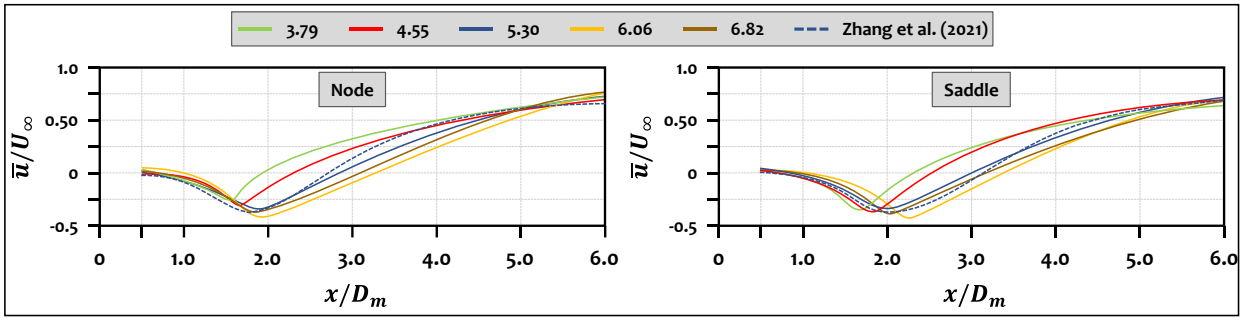


Fig. 13. Mean streamwise velocity distributions along the centerline of the DW cylinder for $\lambda/D_m = 3.79-6.82$ at $Re = 3.9\times10^3$.

3.4Vortex formation lengths

The force coefficients and wake pressures exerted by the fluid flow on the cylinders are significantly affected by the vortex formation length (L_F). The waviness of the geometric surface and shape modifications of the cylinders is responsible for the elongation of L_F (Jung and Yoon, 2014). In this study, the L_F is defined as "the distance from the center point of the cylinder to the point of $u/U_\infty = 0$ along the centerline of the wake." The comparison of non-dimensional vortex formation length (L_F/D) for SC, SW, and DW cylinders for $\lambda/D_m = 3.79-6.82$ at $Re = 3.9\times10^3$ with fixed $a/D_m = 0.152$ is presented in Fig. 14.

Compared with the SC cylinder, the L_F is lengthened for both SW and DW cylinders. The L_F vary along the wavy cylinders' spanwise direction. For SW cylinders, the L_F at nodal planes are extended more than the saddle plane in all cases, which agrees well with Lam and Lin (2009). However, for DW cylinders, the L_F at saddle planes is longer than the nodal planes, which is consistent with Lam et al. (2004b) and Zhang et al. (2021). The maximum value of L_F is found to be 3.41D in the saddle plane of the DW cylinder with $\lambda/D_m = 6.06$, whereas it is found to be 2.97D for the SW cylinder. It can be observed that as λ/D_m increases, the L_F increases until $\lambda/D_m = 6.06$ and then L_F decreases further with increasing in λ/D_m as shown in Fig. 14. As mentioned by Bearman (1965), the L_F is inversely related to the coefficient of base suction pressure ($\bar{C}_{Pb}$). Consequently, for longer L_F, $\bar{C}_{Pb}$ decreases. At the current Reynolds number, i.e., at the subcritical regime, the drag coefficient (C_D) is directly proportional to $\bar{C}_{Pb}$. This means that as the L_F increases, then $\bar{C}_{Pb}$ decreases, which in turn reduces the C_D. Therefore, cylinders with longer L_F have reduced the C_D. Thus, cylinders longer L_F shed alternate eddies further downstream of the cylinder. This alternate shedding of the eddies produces pressure fluctuations on opposite sides of the cylinder. As the eddies shed further from the base of the cylinder, the lift fluctuations become smaller. Based on this, it can be concluded that the wavy cylinders with longer L_F in wake of the cylinders are beneficial to reduce drag and controlling lift fluctuations.

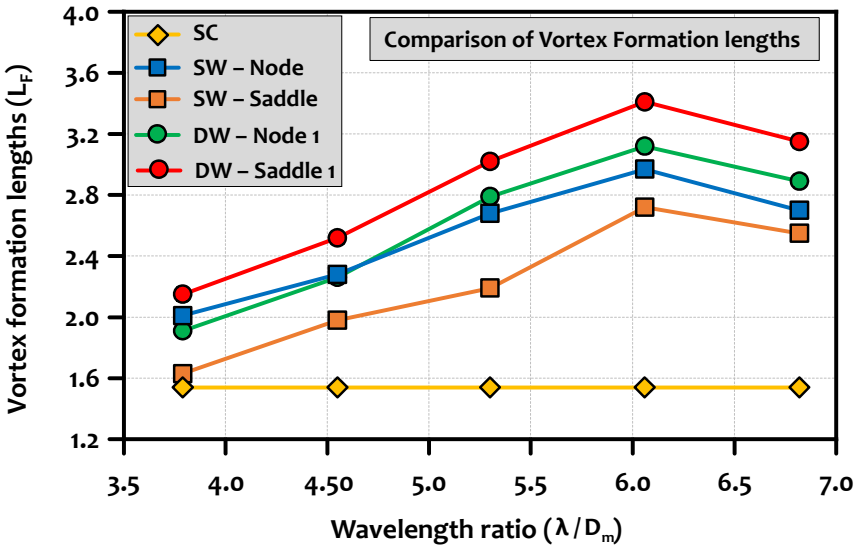


Fig. 14. Comparison of vortex formation lengths for SC, SW, and DW cylinders for various λ/D_m at $Re = 3.9\times10^3$ with fixed $a/D_m = 0.152$.

3.5 Pressure coefficients

The pressure coefficient leads the total forces acting on the cylinders at a given Re. At a large Re, the surface pressure is used to compute drag and lift coefficients. Hence it is essential to investigate the pressure distribution along the periphery of the cylinders. The mean pressure coefficients ($\overline{C}_P$) along with the cylinder circumferential direction (θ) for distinct locations on the cylinder (saddle and nodal planes) for the DW cylinder are depicted in Fig. 15. In every case, the maximum $\overline{C}_P$ occurred at the stagnation point at which the wall shear stress is zero (Williamson, 1988). From the point of stagnation, the $\overline{C}_P$ dramatically declines for all cases reaching minimum value (negative value) at $\theta \approx 72° - 90°$, causing in the establishment of a beneficial pressure gradient ($\partial p/\partial x < 0$) (Zhang et al., 2021) and then slightly increasing as shown in Fig. 15. In this rehabilitation zone, the adverse pressure gradient hindered the boundary layer which lead to the boundary layer separation. It can be observed that the $\overline{C}_P$ remained almost steady after $\theta > 98°$. These patterns of variation of $\overline{C}_P$ for SW and DW cylinders are consistent with Xu et al. (2010) and Zhang et al. (2021).

The variations of the $\overline{C}_P$ for DW cylinder for different λ/D_m at $Re = 3.9 \times 10^3$ are presented in Fig. 15. The $\overline{C}_P$ drastically decreased from the stagnation point and attained a maximum negative value at $\theta > 72°$ for nodal planes and $\theta > 66°$ for saddle planes which can be observed in Fig. 15, For all DW cylinders, this indicates that saddle plane separation occurs earlier than nodal plane separation. The maximum negative $\overline{C}_P$ for the SC cylinder occurred at $\theta = 78°$ which is slightly greater than the value noted for the DW cylinder. The maximum negative value of $\overline{C}_P$ at saddle planes is always greater than at nodal planes for a given λ/D_m. The point of maximum negative pressure coefficient for DW cylinders is always less than the smooth circular cylinder. After $\theta = 98°$, the $\overline{C}_P$ remains almost unchanged as the effect of the boundary layer is negligible and separated from the cylinder surface. It can be found that the $\overline{C}_P$ of DW cylinder at each λ/D_m is greater than the SC cylinder. As the λ/D_m increases, the $\overline{C}_P$ decrease and minimum $\overline{C}_P$ are observed for $\lambda/D_m = 6.06$. The differences in the $\overline{C}_P$ between SC and DW cylinders result in the reduction of drag coefficient by wavy cylinders, which agrees well with Lin et al. (2016) and Chen et al. (2022). Lam and Lin (2008) found that the lengths of velocity recovery of both circular and wavy cylinders are inversely proportional to $\overline{C}_P$. This can be supported by vortex formation lengths presented in Section 3.4, where the SC cylinder has the shortest vortex formation length,

while the DW cylinder with $\lambda/D_m = 6.06$ has the longer vortex formation length as shown in Fig. 14.

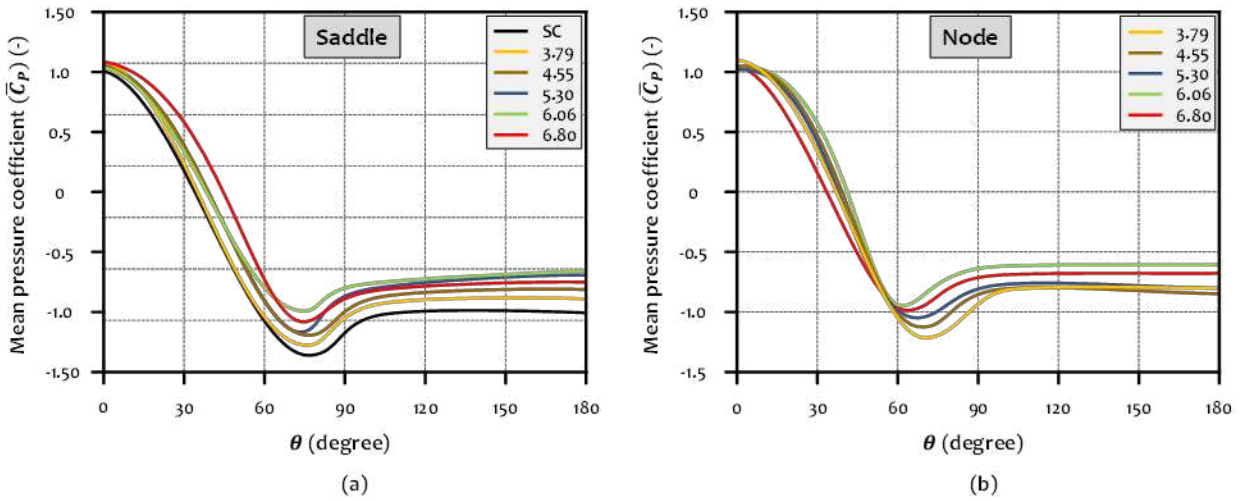


Fig. 15. Variation of mean pressure coefficients ($\bar{C}_P$) (a) Saddle – DW, (b) Node – DW cylinders for different λ/D_m at $Re = 3.9\times10^3$.

4 Conclusions

The flow characteristics of wavy cylinders with single and double waviness are investigated by using LES at $Re = 3.9\times10^3$ for $\lambda/D_m = 3.79 - 6.82$ and fixed $a/D_m = 0.152$. For comparison purposes, the flow past a smooth circular cylinder is also investigated. The mechanisms of flow around wavy cylinders are investigated from the perspective of drag and lift fluctuation reductions. The findings of this study are as follows:

- The mean drag coefficient was reduced by the wavy cylinders compared to smooth circular cylinders due to the high-pressure distribution in the base region of the cylinders at $Re = 3.9\times10^3$.
- The DW cylinder with $\lambda/D_m = 6.06$ reduced more drag coefficient than other cases when compared with the SW cylinder. It reduced drag by 3.94% and 14.13% compared to SW and SC cylinders, respectively.
- The lift fluctuations were almost suppressed by the SW and DW cylinders, as the wavy surfaces of the cylinders reduced the pressure fluctuations. The DW cylinder reduced the lift coefficients by 29.86% and 89.12% compared to the SW and SC cylinders, respectively.
- The shear layers of the DW cylinder cases are more stable than those of the SW and SC cylinders and become further destabilized downstream of the cylinder, resulting in the

formation of elongated wakes and longer vortex formation lengths. Among all cases considered in this study, DW cylinder with $\lambda/D_m = 6.06$ produced longer vortex formation length.

- The pressure coefficients on the saddle and nodal planes differ for wavy cylinders. Due to the longer vortex formation length and its considerable impact on wake pressure, the pressure coefficient decreases, and thereby the forces acting on the cylinders decrease.
- Evidently, the spanwise aligning of these supplemental vortices and thereby their role in the modification of the near wake structures are reliant on the wavelength and amplitude of the geometric surface of the wavy cylinders.

From the above findings, it can be concluded that the flow wake properties were greatly influenced by waviness in the spanwise direction of cylinders in a beneficial way. The SW and DW cylinders with $\lambda/D_m = 6.06$ have shown greater potential to reduce the hydrodynamic coefficients pas the cylinders. Even though the wavy cylinders are rarely used in industrial applications, many previous researchers and recent studies have demonstrated their potential to counteract the hydrodynamic and aerodynamic forces acting on structures at a given Reynolds number. However, more studies are required to investigate the dynamic responses at large Reynolds numbers with different amplitude ratios of wavy cylinders.

Credit authorship contribution statement

Malakonda Reddy Lekkala: Writing – review & editing, Writing – original draft, Visualization, Methodology, Investigation, Formal analysis. **Mohamed Latheef :** Writing – review & editing, Conceptualization, Supervision, Methodology, Investigation, Data curation. **Do Kyun Kim:** Writing – review & editing, Supervision, Project administration, Funding acquisition, Conceptualization. **Ameen Topa**: Writing – review, Methodology, Investigation, Validation.

Acknowledgment

This study was conducted through the international collaboration of several institutions. This work was undertaken at Ocean and Shore Technology (OST) research group and was supported by the National Research Foundation of Korea (2022K2A9A2A2300266). he authors also appreciate the technical support by Dr. Jae Hwan Jung.

References

Ahmed, A. and Bays-Muchmore, B., 1992. Transverse flow over a wavy cylinder. Physics of Fluids A: Fluid Dynamics, 4(9), pp.1959-1967. https://doi.org/10.1063/1.858365.

Assi, G.R., Bearman, P.W. and Kitney, N., 2009. Low drag solutions for suppressing vortex-induced vibration of circular cylinders. Journal of Fluids and Structures, 25(4), pp.666-675. https://doi.org/ 10 .1016/j.jfluidstructs.2008.11.002.

Bearman, P.W., 1965. Investigation of the flow behind a two-dimensional model with a blunt trailing edge and fitted with splitter plates. Journal of fluid mechanics, 21(2), 241-255. https://doi.org/10.1017/ S0022112065000162.

Bearman, P.W. and Owen, J.C., 1998. Reduction of bluff-body drag and suppression of vortex shedding by the introduction of wavy separation lines. Journal of Fluids and Structures, 12(1), pp.123-130. https://doi.org/10.1006/jfls.1997.0128.

Chen, B., Yang, X., Chen, G., Tang, X., Ding, J. and Weng, P., 2022. Numerical study on the flow and noise control mechanism of wavy cylinder. Physics of Fluids, 34(3), p.036108. https:// doi.org/10. 1063/5.0082896.

Choi, H., Jeon, W.P. and Kim, J., 2008. Control of flow over a bluff body. Annu. Rev. Fluid Mech., 40, pp.113-139. https://doi.org/10.1146/annurev.fluid.39.050905.110149.

Darekar, R.M. and Sherwin, S.J., 2001. Flow past a square-section cylinder with a wavy stagnation face. Journal of Fluid Mechanics, 426, pp.263-295. https://doi.org/10.1017/S00221120000 02299.

Deardorff, J.W., 1970. A numerical study of three-dimensional turbulent channel flow at large Reynolds numbers. Journal of Fluid Mechanics, 41(2), pp.453-480. https://doi.org/10.1017/S00221120 70 000691.

Deng, K., Bai, H. and Alam, M.M., 2026. Flow over a bio-inspired wavy elliptic cylinder at a subcritical Reynolds number of 3× 103. Physics of Fluids, 38(2). https://doi.org/10.1063 /5.0310085.

Franke, J. and Frank, W., 2002. Large eddy simulation of the flow past a circular cylinder at Re_D= 3900. Journal of wind engineering and industrial aerodynamics, 90(10), pp.1191-1206. https://doi.org/10.1016 /S0167-6105(02)00232-5.

Jeong, J. and Hussain, F., 1995. On the identification of a vortex. Journal of fluid mechanics, 285, pp.69-94. https://doi.org/10.1017/S0022112095000462.

Germano, M., Piomelli, U., Moin, P. and Cabot, W.H., 1991. A dynamic subgrid-scale eddy viscosity model. Physics of Fluids A: Fluid Dynamics, 3(7), pp.1760-1765. https://doi.org/10.1063 /1.857955.

Gerrard, J.H., 1978. The wakes of cylindrical bluff bodies at low Reynolds number. Philosophical Transactions of the Royal Society of London. Series A, Mathematical and Physical Sciences, 288(1354), pp.351-382. https://doi.org/10.1098/rsta.1978.0020.

Jung, J.H. and Yoon, H.S., 2014. Large-eddy simulation of flow over a twisted cylinder at a subcritical Reynolds number. Journal of fluid mechanics, 759, pp.579-611. https://doi.org/10. 1017/jfm.2014.581.

Karthik, K., Jeyakumar, S. and Sebastin, J.S., 2021. Optimization of wavy cylinder for aerodynamic drag and aeroacoustic sound reduction using computational fluid dynamics analysis. Proceedings of the Institution of Mechanical Engineers, Part C: Journal of Mechanical Engineering Science, 235(11), pp.1979-1991. https://doi.org/10.1177%2F0954406220950353.

Lam, K. and Lin, Y.F., 2007. Drag force control of flow over wavy cylinders at low Reynolds number. Journal of mechanical science and technology, 21(9), p.1331. https://doi.org/10.1007/ BF03177417.

Lam, K. and Lin, Y.F., 2008. Large eddy simulation of flow around wavy cylinders at a subcritical Reynolds number. International Journal of Heat and Fluid Flow, 29(4), pp.1071-1088. https:// doi.org/10. 1016/j.ijheatfluidflow.2008.01.006.

Lam, K., Lin, Y.F., Zou, L. and Liu, Y., 2010. Investigation of turbulent flow past a yawed wavy cylinder. Journal of Fluids and Structures, 26(7-8), pp.1078-1097. https://doi.org/10.1016/ j.jfluidstructs.2010 .07.005.

Lam, K., Wang, F.H., Li, J.Y. and So, R.M.C., 2004a. Experimental investigation of the mean and fluctuating forces of wavy (varicose) cylinders in a cross-flow. Journal of fluids and structures, 19(3), pp.321-334. https://doi.org/10.1016/j.jfluidstructs.2003.12.010.

Lam, K., Wang, F.H. and So, R.M.C., 2004b. Three-dimensional nature of vortices in the near wake of a wavy cylinder. Journal of fluids and structures, 19(6), pp.815-833. https://doi.org/10. 1016/j.jfluidstructs .2004.04.004.

Lekkala, M.R., Mohamed, L., Jung, J.H., Jin, C.K., Li, B., Jeong, B. and Kim, D.K., 2023. Numerical investigations of flow over wavy cylinders at sub-critical Reynolds number. Ocean Engineering, 269, p.113501. https://doi.org/10.1016/j.oceaneng.2022.113501.

Lekkala, M.R., Latheef, M., Jung, J.H., Coraddu, A., Zhu, H., Srinil, N., Lee, B.H. and Kim, D.K., Recent advances in understanding the flow over bluff bodies with different geometries at moderate Reynolds numbers. Ocean Engineering. http://doi.org/10.1016/j.oceaneng. 2022.111611.

Lee, S.J. and Nguyen, A.T., 2007. Experimental investigation on wake behind a wavy cylinder having sinusoidal cross-sectional area variation. Fluid Dynamics Research, 39(4), p.292. https://doi.org/10.101 6/j.fluiddyn.2006.06.003.

Lin, Y.F., Bai, H.L., Alam, M.M., Zhang, W.G. and Lam, K., 2016. Effects of large spanwise wavelength on the wake of a sinusoidal wavy cylinder. Journal of fluids and structures, 61, pp.392-409. https://doi.org/10.1016/j.jfluidstructs.2015.12.004.

Lin, Z.O.U. and Lin, Y.F., 2009. Force reduction of flow around a sinusoidal wavy cylinder. Journal of Hydrodynamics, Ser. B, 21(3), pp.308-315. https://doi.org/10.1016/S1001-6058(08)60151-1.

Lübcke, H., Rung, T. and Thiele, F., 2001. Comparison of LES and RANS in bluff-body flows. Journal of wind engineering and industrial aerodynamics, 89(14-15), pp.1471-1485. https://doi.org/10.1016/S0167-6105(01)00134-9.

Smagorinsky, J., 1963. General circulation experiments with the primitive equations: I. The basic experiment. Monthly weather review, 91(3), pp.99-164. https://doi.org/10.1175/1520-0493(1963)0 91%3C0099:GCEWTP%3E2.3.CO;2.

Williamson, C.H.K., 1988. The existence of two stages in the transition to three-dimensionality of a cylinder wake. The Physics of fluids, 31(11), pp.3165-3168. https://doi.org/10.1063/1.866925.

Xu, C.Y., Chen, L.W. and Lu, X.Y., 2010. Large-eddy simulation of the compressible flow past a wavy cylinder. Journal of Fluid Mechanics, 665, pp.238-273. https://doi.org/10.1017/S0022 112010003927.

Yoon, H.S., Oh, K.J., Kim, H.J., Kim, M.I. and Moon, J., 2020. Double wavy geometric disturbance to the bluff body flow at a subcritical Reynolds number. Ocean Engineering, 195, p.106713. https:// doi.org /10.1016/j.oceaneng.2019.106713.

Zhang, K., Katsuchi, H., Zhou, D., Yamada, H. and Han, Z., 2016. Numerical study on the effect of shape modification to the flow around circular cylinders. Journal of Wind Engineering and Industrial Aerodynamics, 152, pp.23-40. https://doi.org/10.1016/j.jweia.2016.02.008.

Zhang, W. and Lee, S.J., 2005. PIV measurements of the near-wake behind a sinusoidal cylinder. Experiments in fluids, 38(6), pp.824-832. https://doi.org/10.1007/s00348-005-0981-9.

Zhang, Z., Tu, J., Zhang, K., Yang, H., Han, Z., Zhou, D., Xu, J. and Zhang, M., 2021. Vortex characteristics and flow-induced forces of the wavy cylinder at a subcritical Reynolds number. Ocean Engineering, 222, p.108593. https://doi.org/10.1016/j.oceaneng.2021.108593.

Zhao, R., Xu, J.L., Yan, C. and Yu, J., 2011. Scale-adaptive simulation of flow past wavy cylinders at a subcritical Reynolds number. Acta Mechanica Sinica, 27(5), p.660. https://doi.org/10.1007/s10409-011-0490-4.

Zhuang, Y.Q., Sun, X.J. and Huang, D.G., 2018. Numerical study of unsteady flows past a rotating wavy cylinder. European Journal of Mechanics-B/Fluids, 72, pp.538-544. https://doi.org/10.1016/j.euromech flu.2018.07.017.

Zou, L., Guo, C. and Xiong, C., 2013. Flow characteristics of the two tandem wavy cylinders and drag reduction phenomenon. Journal of Hydrodynamics, 25(5), pp.737-746. https://doi.org/10.1016/S1001-6058(13)60420-5.